

Article

Densification and Proton Conductivity of $\text{La}_{1-x}\text{Ba}_x\text{ScO}_{3-\delta}$ Electrolyte Membranes

Alyona Lesnichyova ^{1,2}, Semyon Belyakov ³, Anna Stroeva ⁴, Sofia Petrova ⁵, Vasiliy Kaichev ⁶
and Anton Kuzmin ^{1,4,*}

- ¹ Laboratory of Solid-State Chemistry, Institute of Solid-State Chemistry and Mechanochemistry SB RAS, 630128 Novosibirsk, Russia
² NANOTECH Centre, Ural Federal University, 620075 Yekaterinburg, Russia
³ Laboratory of Electrochemical Materials Science, Institute of High-Temperature Electrochemistry UB RAS, 620137 Yekaterinburg, Russia
⁴ Department of Technology of Inorganic Materials and Electrochemical Production, Vyatka State University, 610000 Kirov, Russia
⁵ Laboratory of High-Entropy Alloys, Institute of Metallurgy UB RAS, 620016 Yekaterinburg, Russia
⁶ Department of Catalysis Research, Boreskov Institute of Catalysis SB RAS, 630090 Novosibirsk, Russia
* Correspondence: a.v.kuzmin@yandex.ru

Abstract: Bain $\text{La}_{1-x}\text{Ba}_x\text{ScO}_{3-\delta}$ impairs sintering and leads to a decrease in its ceramic density. Two approaches have been studied for obtaining dense ceramics: using a high processing temperature and the introduction of a Co_3O_4 sintering additive. An addition of only 0.5 wt% of Co_3O_4 sintering additive, despite the positive sintering effect, causes a noticeable violation of stoichiometry, with partial decomposition of the material. This can lead to the formation of cationic vacancies, which form associates with oxygen vacancies and significantly reduce the oxygen ion and proton conductivity of the materials. There is also a partial substitution of Co for Sc in $\text{La}_{1-x}\text{Ba}_x\text{ScO}_{3-\delta}$, which reduces the stability of protons: it reduces the enthalpy of the hydration reaction, but increases the mobility of protons. Thus, the Co_3O_4 sintering additive causes a complex of negative effects on the conductivity of $\text{La}_{1-x}\text{Ba}_x\text{ScO}_{3-\delta}$ materials. Only high-temperature (1800 °C) processing with protection against Ba loss contributes to the production of dense $\text{La}_{1-x}\text{Ba}_x\text{ScO}_{3-\delta}$ ceramics. The chemical composition of such ceramics corresponds well to the specified one, which ensures high water uptake and, consequently, high proton conductivity.

Keywords: proton conductivity; lanthanum scandate; sintering additive



Citation: Lesnichyova, A.; Belyakov, S.; Stroeva, A.; Petrova, S.; Kaichev, V.; Kuzmin, A. Densification and Proton Conductivity of $\text{La}_{1-x}\text{Ba}_x\text{ScO}_{3-\delta}$ Electrolyte Membranes. *Membranes* **2022**, *12*, 1084. <https://doi.org/10.3390/membranes12111084>

Academic Editors: Byungchan Bae and Natalia Pismenskaya

Received: 3 October 2022

Accepted: 29 October 2022

Published: 31 October 2022

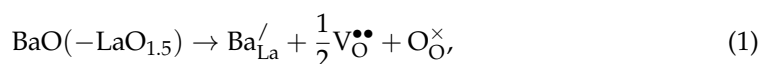
Publisher's Note: MDPI stays neutral with regard to jurisdictional claims in published maps and institutional affiliations.



Copyright: © 2022 by the authors. Licensee MDPI, Basel, Switzerland. This article is an open access article distributed under the terms and conditions of the Creative Commons Attribution (CC BY) license (<https://creativecommons.org/licenses/by/4.0/>).

1. Introduction

Materials with proton conductivity are currently one of the most interesting among solid oxide materials. Among proton-conducting oxides, the highest proton conductivity is realized in acceptor-doped materials with a perovskite-type structure, which makes them promising for use in electrochemical devices, for example, as solid electrolytes for proton–ceramic fuel cells, gas sensors, etc. [1–8]. Their feature is that proton charge carriers are formed by incorporating water vapor into oxygen vacancies, formed, for example, by introducing a cationic acceptor dopant with a reduced valence:



where Ba'_{La} are Ba dopant atoms in La regular lattice positions, $\text{O}_{\text{O}}^{\times}$ are oxygen atoms in regular lattice positions, $\text{V}_{\text{O}}^{\bullet\bullet}$ are oxygen vacancies, and $\text{OH}_{\text{O}}^{\bullet}$ are proton defects.

The perovskite group of the $\text{A}^{3+}\text{B}^{3+}\text{O}_3$ type, such as $\text{La}_{1-x}\text{M}_x\text{BO}_{3-\delta}$ (where $\text{M} = \text{Ca}, \text{Sr}, \text{Ba}; \text{B} = \text{Y}, \text{Yb}, \text{Sc}, \text{In}$) [8–27], are promising ceramic proton conductors because they have

a significant advantage over the widely studied materials based on $\text{Ba}(\text{Zr,Ce})\text{O}_3$ due to the tendency of Ba to carbonize [28–30]. Systematic studies of the transport properties of $\text{La}_{1-x}\text{M}_x\text{BO}_{3-\delta}$ demonstrate a tendency for an increase in proton conductivity with an increase in the ionic radius of the dopant and a decrease in the ionic radius of the B-cation [8–27]; thus, the highest proton conductivity should be realized in $\text{La}_{1-x}\text{Ba}_x\text{ScO}_{3-\delta}$.

Unfortunately, there is no information on $\text{La}_{1-x}\text{Ba}_x\text{ScO}_{3-\delta}$ ceramic sintering in the literature. Lee et al. [15] do not provide information on the density of $\text{La}_{1-x}\text{Ba}_x\text{ScO}_{3-\delta}$ ($x = 0.05\text{--}0.50$) ceramics sintered at $1600\text{ }^\circ\text{C}$ (10 h), despite the fact that the crystal structure and conductivity of these materials have been studied in detail in a wide range of Ba concentrations. They showed a change in the crystal structure when the concentration of Ba increases, namely: at $0 \leq x < 0.1$, an orthorhombic structure is formed, at $0.1 \leq x < 0.3$, a mixture of orthorhombic and cubic is formed, and at $0.3 \leq x \leq 0.5$, only a cubic structure is presented. Kendrick et al. [31] carried out multiple anneals at $1500\text{ }^\circ\text{C}$ (10 h) to prepare single-phase $\text{La}_{0.6}\text{Ba}_{0.4}\text{ScO}_{3-\delta}$, but obtained an actual Ba content of 0.27 and an orthorhombic structure, as well as an impurity of Sc_2O_3 , which is detectable only due to the neutron diffraction technique.

On the example of $\text{La}_{1-x}\text{Ba}_x\text{YbO}_{3-\delta}$, it was shown that even the use of a small amount of Ba can complicate the sintering of ceramics. Kasyanova et al. [26] showed that the sintering of $\text{La}_{1-x}\text{Ba}_x\text{YbO}_{3-\delta}$ ($x = 0.03\text{--}0.1$) ceramics significantly deteriorates at $1400\text{ }^\circ\text{C}$ (5 h) at a concentration of Ba $x \geq 0.05$. On the other hand, Obukuro et al. [27] demonstrated the production of high-density ceramics (more than 95%) of $\text{La}_{1-x}\text{Ba}_x\text{YbO}_{3-\delta}$ ($x = 0.02\text{--}0.1$) after multistage synthesis and long-term sintering (10 h) at $1700\text{ }^\circ\text{C}$, although the authors did not check the Ba losses.

An alternative way to improve the sinterability of ceramics can be the introduction of small amounts of sintering additives, most often, transition metal oxides, into the pre-synthesized powder [32,33]. However, the sintering additive can negatively affect the water uptake and ionic conductivity of Ba-doped LaScO_3 , as shown in recent studies for $\text{Ba}(\text{Zr,Ce,Y})\text{O}_3$ materials [34–37]. The incorporation of over-stoichiometric transition metal atoms into the crystal lattice of proton-conducting materials generally has a negative effect on hydration, in particular, by reducing the saturation limit of protons. According to a study by Han et al. [33], oxides of Co and Ni in the Mn-Fe-Co-Ni series have the least negative effect on the proton transport of $\text{Ba}(\text{Zr,Y})\text{O}_3$ materials. We have previously identified Co_3O_4 among transition metal oxides as the optimal sintering additive for $\text{La}_{0.9}\text{Sr}_{0.1}\text{ScO}_{3-\delta}$ [8], while the effect of the same additive on $\text{La}_{1-x}\text{Ba}_x\text{ScO}_{3-\delta}$ has not been studied.

In this research, we investigated the effect of heat treatment regimes, as well as 0.5 wt% Co_3O_4 , on the sintering process and microstructure, crystal structure, water uptake, and proton conductivity of the $\text{La}_{1-x}\text{Ba}_x\text{ScO}_{3-\delta}$ proton-conducting materials.

2. Materials and Methods

Materials of composition $\text{La}_{1-x}\text{Ba}_x\text{ScO}_{3-\delta}$ (where $x = 0.025, 0.05, 0.075, \text{ and } 0.1$) were synthesized using the citrate–nitrate combustion method. Oxides La_2O_3 and Sc_2O_3 , and carbonate BaCO_3 (all of high pure grade), were used as precursors. Stoichiometric amounts of precursors, taking into account their weight loss coefficients during calcination, were converted to a nitrate solution using a nitric acid. After complete dissolution of all precursors, citric acid was added to the resulting mixture and evaporated until the combustion reaction proceeded. The powders obtained after drying were annealed at a temperature of $800\text{ }^\circ\text{C}$ for 2 h for decarbonization, after which the powder mixture was homogenized in isopropyl alcohol using a PM 100 zirconia-based planetary ball mill (Retch GmbH, Haan, Germany) for 1 h (350 rpm). Dried powders of all compositions were subjected to preliminary synthesis at $1200\text{ }^\circ\text{C}$ for 2 h. Parallel to the above path, 0.5 wt% Co_3O_4 (high pure grade) was added above the basic stoichiometry to the $\text{La}_{0.95}\text{Ba}_{0.05}\text{ScO}_{3-\delta}$ powder obtained after annealing at $800\text{ }^\circ\text{C}$, after which this mixture was homogenized in the planetary ball mill for 1 h (350 rpm) and calcined in air at $1200\text{ }^\circ\text{C}$ for 2 h.

From the powders obtained by two above methods, compacts were made using a uniaxial hydraulic press at 400 Pa, which were then covered in the sacrificial powder of the same composition and sintered in air at 1650 °C for 5 h. In the case of sample $\text{La}_{0.95}\text{Ba}_{0.05}\text{ScO}_{3-\delta}$ obtained after two preliminary sintering at 1400 °C (1 h) and 1650 °C (5 h), additional sintering was carried out in a vacuum furnace at 1800 °C for 2 h using a sacrificial powder of the appropriate composition. Then, the obtained ceramic samples were calcined in air at 1100 °C for 5 h for oxygen stoichiometry relaxation. The shrinkage of compacts during heat treatment in air was studied by optical dilatometry using an ODP-868 platform (TA Instruments, New Castle, DE, USA) in the temperature range from room temperature to 1575 °C.

The identification of phases, as well as the crystal structure, was carried out using powder X-ray diffraction (XRD) analysis on a D/MAX-2200 diffractometer (Rigaku, Tokyo, Japan). High-temperature XRD analysis was performed in dry air on a D8 Advance diffractometer (Bruker, Karlsruhe, Germany) with a XRK-900 high-temperature chamber (Anton Paar, Graz, Austria). In both cases, the $\text{Cu K}\alpha$ radiation was used. A dry atmosphere ($p_{\text{H}_2\text{O}} = 0.1$ kPa) was achieved by gas circulation through a column with zeolites. The measurements were carried out in a temperature range from room temperature to 900 °C, in the heating mode with a step of 20 °C and in the cooling mode with a step of 30 °C and with an exposure time of 8 min at each point. Phase analysis was performed using the DIFFRAC^{plus}.EVA software (Bruker, Karlsruhe, Germany) [38] and PDF4 + ICDD database (Release 2021) [39]. The unit cell parameters were calculated using the Celref software (ENSP, Grenoble, France) [40]. Rietveld structure refinement was performed using the DIFFRAC^{plus}.TOPAS software (Bruker, Karlsruhe, Germany) [41].

The cross-sections and surface of the ceramic samples were investigated by scanning electron microscopy (SEM) using MIRA 3 LMU equipment (Tescan, Brno, Czech Republic). The elemental distribution was studied by energy-dispersive X-ray (EDX) spectroscopy using INCA Energy 350 X-Max 80 equipment (Oxford Instruments, Concord, MA, USA).

X-ray photoelectron spectroscopy (XPS) analysis of the samples was carried out on a X-ray photoelectron spectrometer equipped with a hemispherical analyzer PHOIBOS-150-MCD-9 and XR-50 source of X-ray radiation (SPECS Surface Nano Analysis GmbH, Berlin, Germany). The spectra were recorded using nonmonochromatized $\text{Al K}\alpha$ radiation (1486.6 eV). The charge correction was performed by setting the $\text{Sc}2p$ peak at 402.0 eV. The background was subtracted by the Shirley method. Quantitative analysis was performed using the integrated intensities of core-level spectra with the cross-sections according to Scofield [42]. The curve fitting was completed with CasaXPS software (Casa Software Ltd., Teignmouth, UK) [43]. The shape of the peaks is approximated by a symmetric function obtained by multiplying the Gauss and Lorentz functions.

The thermal expansion of the dense ceramic bars was studied using a quartz dilatometer and Tesatronic TT-80 equipment (TESA, Renens, Switzerland) from room temperature to 900 °C with a heating/cooling rate of 2 °C min^{-1} in dry air ($p_{\text{H}_2\text{O}} = 0.1$ kPa).

The thermogravimetric analysis (TGA) was performed on the powder samples with a specific surface area of 1.1 ± 0.2 m^2/g using a STA Jupiter 449 F3 analyzer (Netzsch, Selb, Germany) with an aSTEAM DV2MK (aDROP Feuchtemeßtechnik GmbH, Fürth, Germany) water vapor generator. The as-prepared powders were heated up to 950 °C and held at this temperature for 8 h under the dry argon. Afterwards, the carrier gas was saturated with water vapor ($p_{\text{H}_2\text{O}} = 24.3$ kPa), and then the increase in weight was recorded upon cooling from 950 °C to 300 °C with a cooling rate of 30 °C h^{-1} and exposure every 100 °C over 2 h. The proton concentration was obtained from the weight change during TGA as follows:

$$\Delta n_{\text{OH}} = \frac{2 \cdot \Delta m \cdot M_{\text{s}}}{m_{\text{s}} \cdot M_{\text{H}_2\text{O}}} \quad (3)$$

where M_{s} and $M_{\text{H}_2\text{O}}$ are molecular weights of the oxides and water, and Δm and m_{s} are the weight change and weight of the specimen, respectively.

The total conductivity was measured as a function of the temperature ($T = 900\text{--}400\text{ }^\circ\text{C}$), oxygen partial pressure ($p_{\text{O}_2} = 21.3\text{ kPa}\text{--}10^{-15}\text{ Pa}$), and water partial pressure ($p_{\text{H}_2\text{O}} = 0.1$ and 2.8 kPa) by the four-probe DC method using an ADAM-3000 instrument (Advantech, Taiwan). The samples were rectangular bars with four Pt electrodes, which were made of dispersed Pt powder and sintered at $1100\text{ }^\circ\text{C}$ during 1 h. The p_{O_2} was controlled by an electrochemical oxygen pump and a sensor based on an yttria-stabilized zirconia (YSZ). The partial conductivities of protons, oxygen ions, and holes were calculated on the basis of the dependences of the total conductivity on p_{O_2} and $p_{\text{H}_2\text{O}}$ in the framework of the approach developed by Frade [44] and Baek [45]. A detailed description of the calculations is given in [24]. The experimental dependences of total conductivity on $(p_{\text{O}_2})^{1/4}$, which were obtained at two humidity values 2.8 kPa and 0.1 kPa , were used for the calculations and are given in the Supplementary Materials (Figure S1).

The electrochemical impedance spectroscopy (EIS) was performed at $450\text{--}300\text{ }^\circ\text{C}$ in wet air using a SP-200 m (Bio-Logic, Seyssinet-Pariset, France). The measurements were carried out in a frequency range of $7\text{ MHz}\text{--}500\text{ mHz}$ and at a sinus signal amplitude of 100 mV . The impedance spectra were interpreted into bulk and grain boundary (GB) components using an equivalent circuit scheme of $R_0\text{--}(R_1Q_1)\text{--}(R_2Q_2)$, where R is the resistance, Q is the constant phase element, and the indexes of 1 and 2 correspond to the bulk and GB processes, respectively. R_0 was purposefully introduced in the equivalent circuit scheme; it imitates the origin of the coordinates, providing a correct fitting. In the approximation of equality of the dielectric constants of the bulk and GBs [46], the GB resistance can be converted to a specific value using the formula:

$$\sigma_{\text{gb}}^* = \frac{1}{R_{\text{gb}}} \cdot \frac{1}{S} \cdot \frac{C_{\text{bulk}}}{C_{\text{gb}}}, \quad (4)$$

where R_{gb} is the GB resistance, $\frac{1}{S}$ is the geometric parameter, and C_{bulk} and C_{gb} are the capacities of the bulk and GB, respectively.

3. Results

3.1. Materials Characterization

Figure 1 demonstrates the XRD patterns of prepared and dried powders of $\text{La}_{1-x}\text{Ba}_x\text{ScO}_{3-\delta}$ ($0\text{--}0.1$) obtained by combustion synthesis with final calcination at $1650\text{ }^\circ\text{C}$. The crystal structure of $\text{La}_{1-x}\text{Ba}_x\text{ScO}_{3-\delta}$ was characterized as an orthorhombic perovskite with the $Pnma$ space group. No impurity phases were observed, which corresponds to a wide range of Ba dissolution in LaScO_3 [15]. An increase in the Ba concentration leads to the gradual displacement of Bragg peaks; thus, the unit cell volume of $\text{La}_{1-x}\text{Ba}_x\text{ScO}_{3-\delta}$ increases (Figure 2). This is in a good agreement with the conventional representation of ionic radii by Shannon [47] because the ionic radius of Ba ($r_{\text{Ba}^{2+}} = 1.61\text{ \AA}$) is larger than La ($r_{\text{La}^{3+}} = 1.36\text{ \AA}$). Thus, when Ba replaces La, the crystal lattice of $\text{La}_{1-x}\text{Ba}_x\text{ScO}_{3-\delta}$ undergoes expansion [48] according to the equations:

$$V = 4 \cdot a_p^3, \quad (5)$$

$$a_p = \frac{A}{\sqrt{2}} \cdot ((1-x) \cdot r_{\text{La}} + x \cdot r_{\text{Ba}}) + r_{\text{O}} + B \cdot (r_{\text{Sc}} + r_{\text{O}}) + C, \quad (6)$$

where a_p is the pseudocubic unit cell parameter; A , B , and C are empirical parameters equal to 0.816 , 1.437 , and -0.63095 , respectively [48]; and r_{La} , r_{Ba} , r_{Sc} , r_{O} are Shannon ionic radii of La^{3+} , Ba^{2+} , Sc^{3+} , and O^{2-} [47], respectively. In Figure 2 we can see that the theoretically calculated values of the unit cell volume are in good agreement with the values experimentally determined by XRD. It is important to note that we deliberately dried the samples prior to the XRD analysis in order to prevent additional hydration-related materials expansion.

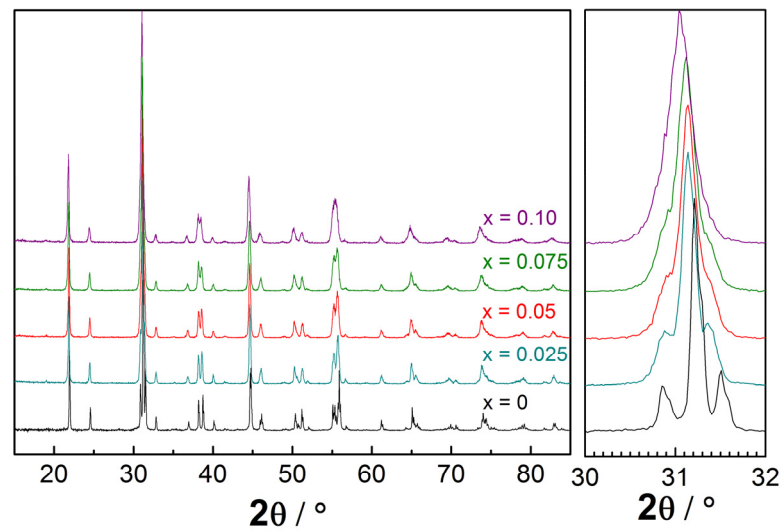


Figure 1. XRD patterns of $\text{La}_{1-x}\text{Ba}_x\text{ScO}_{3-\delta}$ samples.

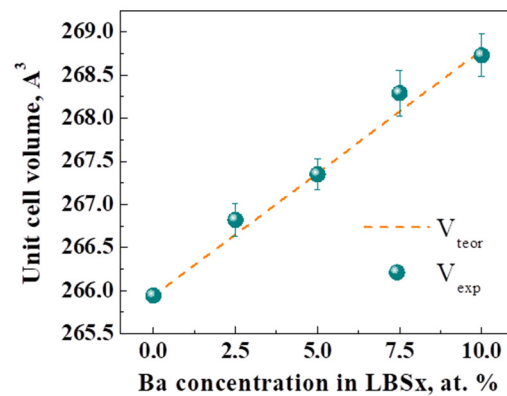


Figure 2. Unit cell volume of $\text{La}_{1-x}\text{Ba}_x\text{ScO}_{3-\delta}$ samples.

According to Figure 3, the relative density of sintered $\text{La}_{1-x}\text{Ba}_x\text{ScO}_{3-\delta}$ ceramic materials decreases from ~94% for $x = 0.025$ to ~76% for $x = 0.1$. The average grain size also decreases with increases in the Ba concentration. Both trends show the deterioration of the sintering of ceramics based on LaScO_3 caused by the presence of Ba, although similar trends were not previously observed for Ca- and Sr-doped LaScO_3 [20,21,24]. Thus, obtaining dense $\text{La}_{1-x}\text{Ba}_x\text{ScO}_{3-\delta}$ ceramic materials is a difficult task, and therefore, taking $\text{La}_{0.95}\text{Ba}_{0.05}\text{ScO}_{3-\delta}$ as an example, we considered various strategies for producing dense ceramics.

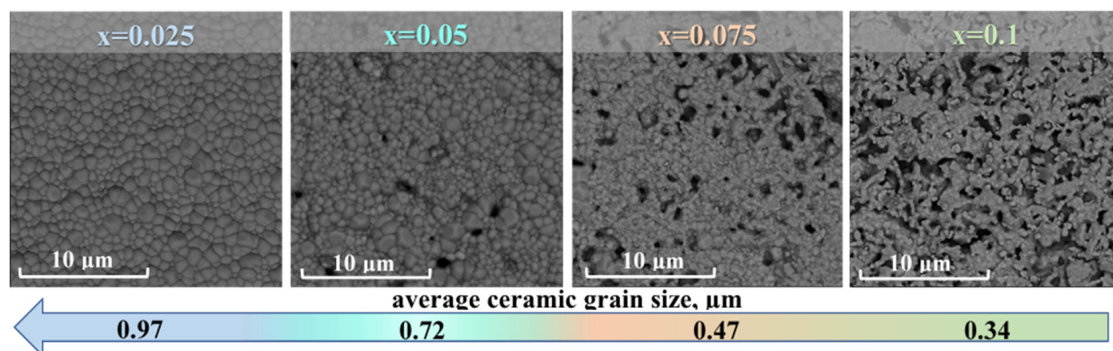


Figure 3. SEM images of surface morphology of $\text{La}_{1-x}\text{Ba}_x\text{ScO}_{3-\delta}$ ceramics.

3.2. Dense Ceramic Formation Strategies

The general scheme for studying the sintering process of $\text{La}_{0.95}\text{Ba}_{0.05}\text{ScO}_{3-\delta}$ samples is shown in Figure 4. As you can see in Figure 5, the most intense stage of shrinkage of $\text{La}_{0.95}\text{Ba}_{0.05}\text{ScO}_{3-\delta}$ occurs up to a temperature of 1420 °C and is only 6% of the initial compact volume. With a further increase in temperature, the shrinkage rate decreases, since the process of grain growth begins to compete with the shrinkage of the material, which leads to the formation of porous ceramics with a relative density of 82% after sintering at 1650 °C over 5 h (Figure 4a).

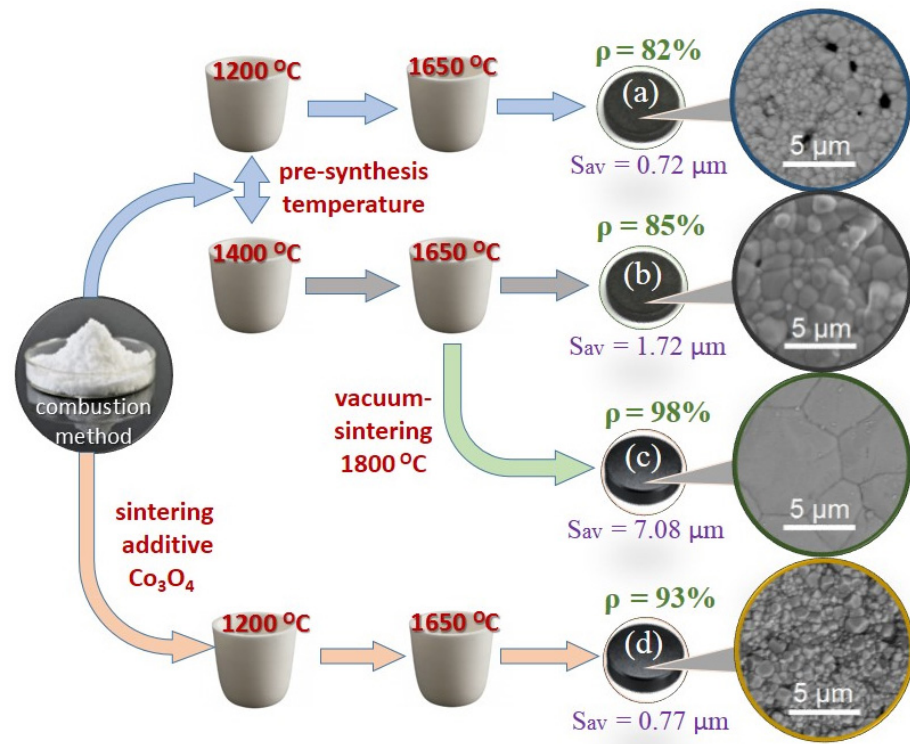


Figure 4. Sintering scheme for $\text{La}_{0.95}\text{Ba}_{0.05}\text{ScO}_{3-\delta}$ ceramics. ρ is the relative density, and S_{av} is the average grain size. The explanation for subfigures are in the text of the paper.

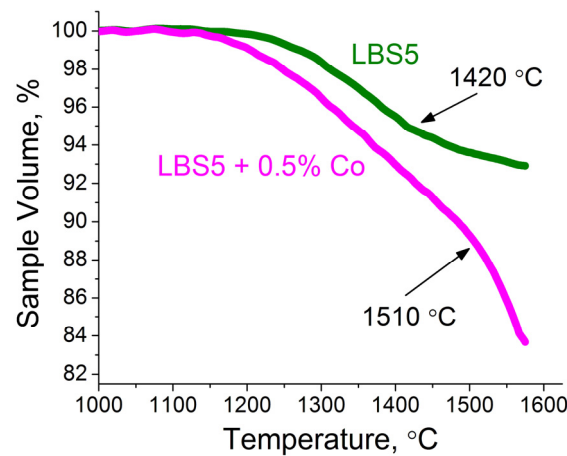


Figure 5. Shrinkage of $\text{La}_{0.95}\text{Ba}_{0.05}\text{ScO}_{3-\delta}$ and $\text{La}_{0.95}\text{Ba}_{0.05}\text{ScO}_{3-\delta} + 0.5 \text{ wt\% Co}_3\text{O}_4$ samples during sintering according to optical dilatometry analysis.

Based on the temperature dependence of shrinkage for $\text{La}_{0.95}\text{Ba}_{0.05}\text{ScO}_{3-\delta}$ samples (Figure 5), the pre-sintering temperature was increased from 1200 to 1400 °C, which led to

an increase in the average grain size of the ceramic to $1.72 \pm 0.42 \mu\text{m}$, while the relative density still does not exceed 85% after $1650 \text{ }^\circ\text{C}$ sintering over 5 h (Figure 4b). This result prompted us to carry out additional sintering in a vacuum furnace, where the temperature reached $1800 \text{ }^\circ\text{C}$ after 2 h. As can be seen from Figure 4c, after vacuum sintering, it was possible to obtain ceramics with a relative density of 98% and an impressive average grain size of $7.08 \pm 1.19 \mu\text{m}$.

We introduced 0.5 wt% Co_3O_4 into the synthesized $\text{La}_{0.95}\text{Ba}_{0.05}\text{ScO}_{3-\delta}$ powder, since it was shown earlier [8] that cobalt oxide is the optimal additive for $\text{La}_{0.9}\text{Sr}_{0.1}\text{ScO}_{3-\delta}$. As Figure 5 shows, the densification process becomes more active with the addition of Co_3O_4 : it begins at $1150 \text{ }^\circ\text{C}$ and reaches 12% at $1510 \text{ }^\circ\text{C}$, and with a further increase in temperature, the sintering rate increases. In this case, the process of grain splicing dominates, which leads to an increase in the density of ceramics up to ~93% after sintering at $1650 \text{ }^\circ\text{C}$ over 5 h (Figure 4d).

3.3. Dense Ceramics Characterization

Figure 6 shows the XRD patterns of $\text{La}_{0.95}\text{Ba}_{0.05}\text{ScO}_{3-\delta}$ crushed ceramics: after standard sintering at $1650 \text{ }^\circ\text{C}$, vacuum sintering at $1800 \text{ }^\circ\text{C}$ and sintering at $1650 \text{ }^\circ\text{C}$ with 0.5 wt% Co_3O_4 sintering additive at $1650 \text{ }^\circ\text{C}$. The perovskite-like structure was confirmed in all cases, and as Table 1 shows, the unit cell parameters for all samples are very similar. In the case of the $\text{La}_{0.95}\text{Ba}_{0.05}\text{ScO}_{3-\delta} + 0.5 \text{ wt}\% \text{Co}_3\text{O}_4$ sample, there are additional XRD peaks that may correspond to $\text{Ba}_2\text{Sc}_2\text{O}_5$ [49] and peroxide BaO_2 impurities.

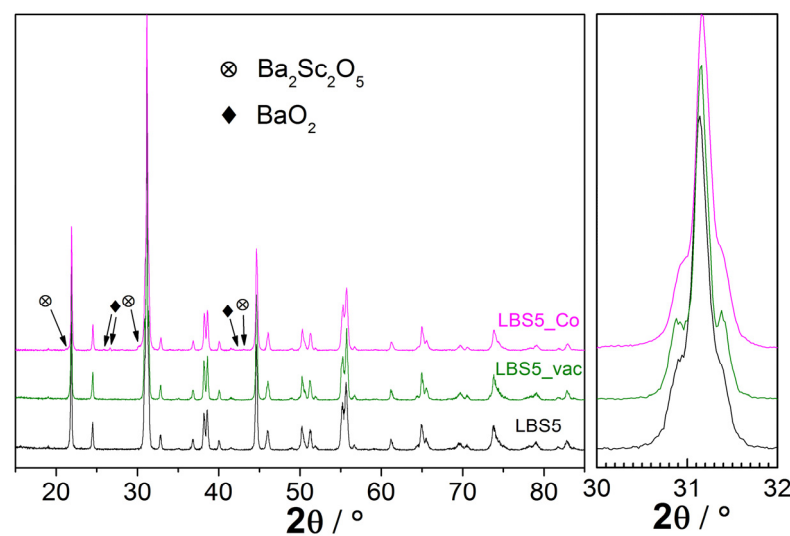


Figure 6. XRD patterns of $\text{La}_{0.95}\text{Ba}_{0.05}\text{ScO}_{3-\delta}$ samples obtained after standard sintering ($1650 \text{ }^\circ\text{C}$), vacuum sintering ($1800 \text{ }^\circ\text{C}$), and sintering with 0.5 wt% Co_3O_4 additive ($1650 \text{ }^\circ\text{C}$).

Table 1. Unit cell parameters of $\text{La}_{0.95}\text{Ba}_{0.05}\text{ScO}_{3-\delta}$ samples sintered in various ways.

Sample	A, Å	B, Å	C, Å	Volume, Å ³
$\text{La}_{0.95}\text{Ba}_{0.05}\text{ScO}_{3-\delta}$ standard sintering	5.780	8.110	5.697	267.1
$\text{La}_{0.95}\text{Ba}_{0.05}\text{ScO}_{3-\delta}$ vacuum $1800 \text{ }^\circ\text{C}$	5.784	8.105	5.692	266.9
$\text{La}_{0.95}\text{Ba}_{0.05}\text{ScO}_{3-\delta} + 0.5 \text{ wt}\% \text{Co}_3\text{O}_4$	5.778	8.106	5.693	266.7

SEM images of cross-sections in Figure 7 demonstrate the absence of closed image pores in the volume of the ceramics. The results of EDX analysis show a homogeneous distribution of La, Ba, and Sc in the vacuum sintered sample (Figure 7a). At the same time, for $\text{La}_{0.95}\text{Ba}_{0.05}\text{ScO}_{3-\delta} + 0.5 \text{ wt}\% \text{Co}_3\text{O}_4$, a small number of regions with an increased Sc concentration are noted (Figure 7b), which may correspond to Sc_2O_3 . We do not detect areas enriched in Ba, indicating a uniform distribution of Ba in terms of EDX beam size. As

seen from Table 2, the quantitative ratio of cations is in good agreement with the nominal compositions of the samples, although a slight deficit in the sum of La and Ba relative to Sc is observed. In this case, the amount of Ba relative to La is in good agreement with the given one and is equal to 0.05; therefore, in this case, the evaporation of Ba during synthesis does not occur even after high-temperature annealing in a vacuum at 1800 °C. Most likely, the use of sacrificial powder led to this good result.

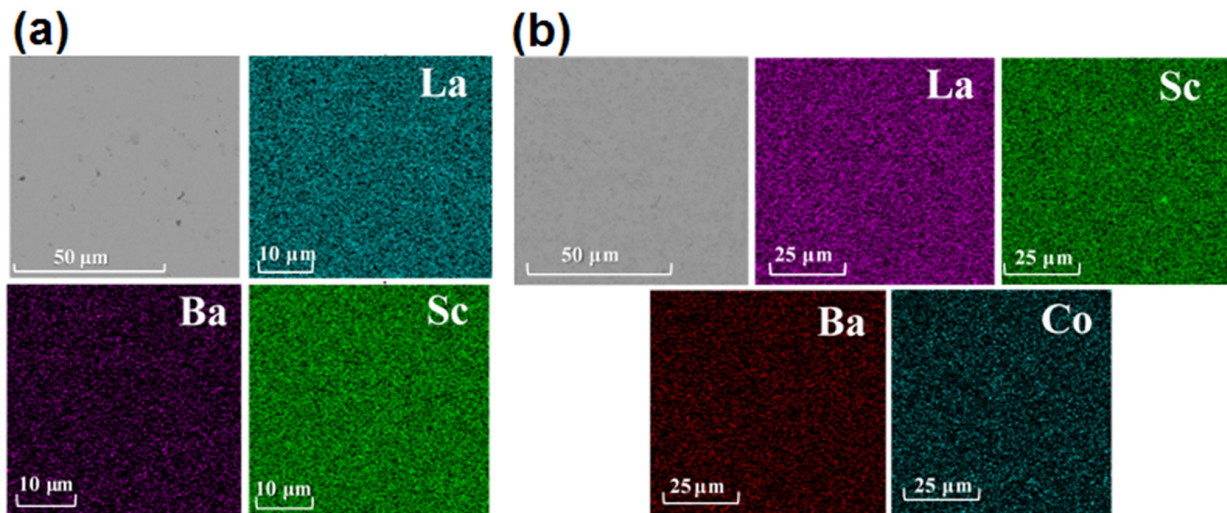


Figure 7. SEM images (BSE mode) of cross-sections for $\text{La}_{0.95}\text{Ba}_{0.05}\text{ScO}_{3-\delta}$ after vacuum sintering (a) and $\text{La}_{0.95}\text{Ba}_{0.05}\text{ScO}_{3-\delta} + 0.5 \text{ wt}\% \text{Co}_3\text{O}_4$ (b) with EDX maps of cation distribution.

Table 2. Element contents (at.% ± 0.05) in the ceramics cross-sections according to EDX analysis.

Sample	La	Ba	Sc	Co	[Ba]/[La]
$\text{La}_{0.95}\text{Ba}_{0.05}\text{ScO}_{3-\delta}$ vacuum 1800 °C	47.25	2.42	50.33	-	0.05
$\text{La}_{0.95}\text{Ba}_{0.05}\text{ScO}_{3-\delta} + 0.5 \text{ wt}\% \text{Co}_3\text{O}_4$	46.87	2.27	49.98	0.88	0.048

Figure 8 shows the $\text{Ba}3d$ and $\text{Co}2p$ core-level spectra of the $\text{La}_{0.95}\text{Ba}_{0.05}\text{ScO}_{3-\delta} + 0.5 \text{ wt}\% \text{Co}_3\text{O}_4$ sample. The $\text{Ba}3d$ spectra split into the $\text{Ba}3d_{5/2}$ and $\text{Ba}3d_{3/2}$ components (the spin-orbital splitting is 15.3 eV) due to the spin-orbit interaction. The $\text{Ba}3d_{5/2}$ binding energy is 780.0 eV, which corresponds to the Ba^{2+} state [50,51]. The $\text{Ba}3d$ and $\text{Co}2p$ spectra overlap substantially. For comparison, we present the data for the $\text{La}_{0.9}\text{Sr}_{0.1}\text{ScO}_{3-\delta} + 0.5 \text{ wt}\% \text{Co}_3\text{O}_4$ sample, which was studied in detail elsewhere [8]. The $\text{Co}2p$ spectra are the $\text{Co}2p_{3/2}$ – $\text{Co}2p_{1/2}$ doublet. Cobalt in the Co^{2+} state is characterized by the $\text{Co}2p_{3/2}$ binding energies in the range 780.0–782.0 eV, as well as the presence of an intense (up to 20% of the main peak) ‘shake-up’ satellite in the 786–787 eV region [52–54]. As seen in Figure 8, the $\text{Co}2p_{3/2}$ is a symmetric peak at 781.0 eV; thus, the $\text{Co}2p$ spectrum for $\text{La}_{0.9}\text{Sr}_{0.1}\text{ScO}_{3-\delta} + 0.5 \text{ wt}\% \text{Co}_3\text{O}_4$ contains only one Co^{2+} component with a small intensity. This indicates that Co atoms diffused into the bulk of the grains. We expect a similar behavior for the $\text{La}_{0.95}\text{Ba}_{0.05}\text{ScO}_{3-\delta} + 0.5 \text{ wt}\% \text{Co}_3\text{O}_4$ sample, which allows for a good fitting of the XPS spectrum as a sum of two components: Ba^{2+} and Co^{2+} (Figure 8). Elemental analysis indicates a threefold excess of Ba ([Ba]/[La] = 0.16) and slight excess of La ([La]/[Sc] = 1.2) on the surface of the sample.

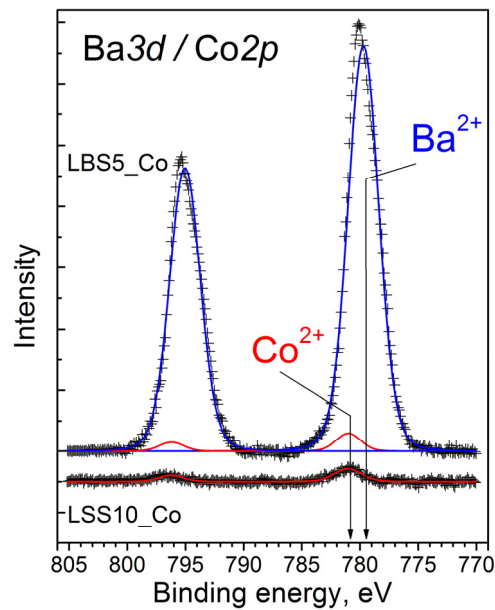


Figure 8. Ba3d (blue line) and Co2p (red line) core-levels spectra of La_{0.95}Ba_{0.05}ScO_{3-δ} + 0.5 wt% Co₃O₄ and La_{0.9}Sr_{0.1}ScO_{3-δ} + 0.5 wt% Co₃O₄ samples.

3.4. Thermal Expansion

As shown in Figure 9, the linear dependence of thermal expansion in a dry air atmosphere according to dilatometry and HT-XRD data indicates the absence of structural transitions. Kim et al. [15] mentioned the formation of a mixture of orthorhombic and cubic phases for La_{1-x}Ba_xScO_{3-δ} with $x \geq 0.1$, while Kendrick et al. [31] definitely indicated an orthorhombic structure for La_{0.73}Ba_{0.27}ScO_{3-δ}. For La_{0.95}Ba_{0.05}ScO_{3-δ}, the orthorhombic structure with the *Pnma* space group is retained up to 900 °C. Dilatometric results show linear expansion of both La_{0.95}Ba_{0.05}ScO_{3-δ} and La_{0.95}Ba_{0.05}ScO_{3-δ} + 0.5 wt% Co₃O₄ ceramic samples with thermal expansion coefficient (TEC) values corresponding to $8.9 \cdot 10^{-6} \text{ K}^{-1}$, which is close to the values for Ca- and Sr-doped LaScO₃ [20,21].

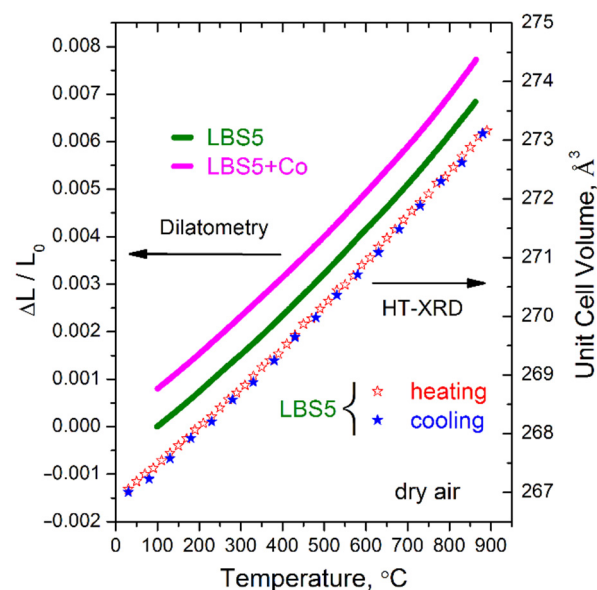


Figure 9. Thermal expansion of La_{0.95}Ba_{0.05}ScO_{3-δ} and La_{0.95}Ba_{0.05}ScO_{3-δ} + 0.5 wt% Co₃O₄ ceramic samples in dry air according to dilatometry and HT-XRD.

3.5. Water Uptake

According to Equations (1) and (2), the value of maximal water uptake (x_{ef} , saturation limit) has to be equal to the Ba acceptor dopant concentration $n_{OH} = 0.05$ for the investigated $\text{La}_{0.95}\text{Ba}_{0.05}\text{ScO}_{3-\delta}$ sample. Figure 10 demonstrates the temperature dependence of the proton concentration in $\text{La}_{0.95}\text{Ba}_{0.05}\text{ScO}_{3-\delta}$ and $\text{La}_{0.95}\text{Ba}_{0.05}\text{ScO}_{3-\delta} + 0.5 \text{ wt}\% \text{ Co}_3\text{O}_4$ crushed ceramic samples, which were obtained by TGA. In the case of $\text{La}_{0.95}\text{Ba}_{0.05}\text{ScO}_{3-\delta}$, the proton uptake saturation limit x_{ef} closely approaches the nominal Ba concentration. The calculated thermodynamic parameters of hydration ΔH_{hydr} (standard enthalpy) and ΔS_{hydr} (standard entropy) for $\text{La}_{0.95}\text{Ba}_{0.05}\text{ScO}_{3-\delta}$ were $-85 \pm 6 \text{ kJ mol}^{-1}$ and $-106 \pm 6 \text{ J mol}^{-1} \text{ K}^{-1}$, respectively. These values are more positive than the values of ΔH_{hydr} and ΔS_{hydr} for Ca-doped [21] and Sr-doped [19,23] LaScO_3 at the same concentration of the acceptor dopant. It is found that the proton concentrations for the $\text{La}_{0.95}\text{Ba}_{0.05}\text{ScO}_{3-\delta} + 0.5 \text{ wt}\% \text{ Co}_3\text{O}_4$ sample were significantly below the nominal acceptor concentration. Both $\Delta H_{hydr} = -62 \pm 2 \text{ kJ mol}^{-1}$ and $\Delta S_{hydr} = -89 \pm 2 \text{ J mol}^{-1} \text{ K}^{-1}$ thermodynamic parameters became even more positive for $\text{La}_{0.95}\text{Ba}_{0.05}\text{ScO}_{3-\delta} + 0.5 \text{ wt}\% \text{ Co}_3\text{O}_4$. Thus, the results clearly indicate a negative effect of Co_3O_4 additive on water uptake, both on the concentration of protons and on the hydration thermodynamics.

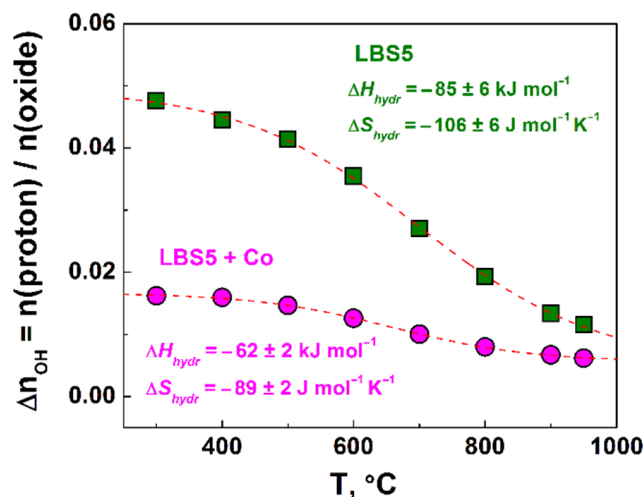


Figure 10. Proton concentrations in $\text{La}_{0.95}\text{Ba}_{0.05}\text{ScO}_{3-\delta}$ and $\text{La}_{0.95}\text{Ba}_{0.05}\text{ScO}_{3-\delta} + 0.5 \text{ wt}\% \text{ Co}_3\text{O}_4$ samples.

3.6. Conductivity

3.6.1. Total Conductivity

Figure 11 shows the temperature dependencies of the total conductivity of the $\text{La}_{0.95}\text{Ba}_{0.05}\text{ScO}_{3-\delta}$ and $\text{La}_{0.95}\text{Ba}_{0.05}\text{ScO}_{3-\delta} + 0.5 \text{ wt}\% \text{ Co}_3\text{O}_4$ samples in oxidizing and reducing atmospheres at $p\text{H}_2\text{O} = 2.8 \text{ kPa}$, measured using the 4-probe DC method. The dependencies in a reducing atmosphere demonstrate a clear inflection caused by the superposition of two types of ion transport: proton and oxygen ion. In an oxidizing atmosphere, they have an almost linear form, which is the result of the three charge carriers' contribution (protons, oxygen ions, and holes). Holes are formed according to the oxidation reaction:



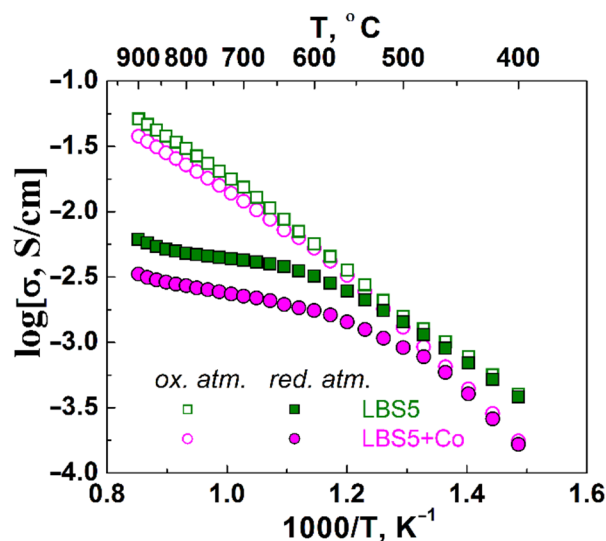


Figure 11. Temperature dependencies of electrical conductivity of $\text{La}_{0.95}\text{Ba}_{0.05}\text{ScO}_{3-\delta}$ and $\text{La}_{0.95}\text{Ba}_{0.05}\text{ScO}_{3-\delta} + 0.5 \text{ wt\% Co}_3\text{O}_4$ ceramics in wet oxidizing and reducing atmospheres.

The predominance of hole conductivity at high temperatures leads to the linearization of the temperature dependence of the total conductivity. The total conductivity values of $\text{La}_{0.95}\text{Ba}_{0.05}\text{ScO}_{3-\delta}$ are higher than those of $\text{La}_{0.95}\text{Ba}_{0.05}\text{ScO}_{3-\delta} + 0.5 \text{ wt\% Co}_3\text{O}_4$, primarily due to the reduced concentration of defects in the latter. The difference in the relative density of the $\text{La}_{0.95}\text{Ba}_{0.05}\text{ScO}_{3-\delta}$ (98%) and $\text{La}_{0.95}\text{Ba}_{0.05}\text{ScO}_{3-\delta} + 0.5 \text{ wt\% Co}_3\text{O}_4$ (93%) materials should also not be ruled out, although it is not as significant as might be expected.

3.6.2. Proton, Oxygen Ion, and Hole Partial Conductivities

Figure 12a shows the temperature dependences of the partial hole, oxygen ion, and proton conductivity in a humid oxidizing atmosphere in the temperature range 800–600 °C. The hole conductivity dominates over oxygen ion and proton conductivity, which is associated with the high mobility of holes, although their concentration is rather low. The hole conductivity of $\text{La}_{0.95}\text{Ba}_{0.05}\text{ScO}_{3-\delta}$ and $\text{La}_{0.95}\text{Ba}_{0.05}\text{ScO}_{3-\delta} + 0.5 \text{ wt\% Co}_3\text{O}_4$ is comparable, although the activation energy for $\text{La}_{0.95}\text{Ba}_{0.05}\text{ScO}_{3-\delta} + 0.5 \text{ wt\% Co}_3\text{O}_4$ (~0.72 eV) is lower compared to that of $\text{La}_{0.95}\text{Ba}_{0.05}\text{ScO}_{3-\delta}$ without sintering additive (~0.89 eV). In contrast to the hole conductivity, the presence of a Co_3O_4 additive leads to a significant decrease in proton and oxygen ion conductivity. The proton mobility was calculated using the formula:

$$\mu_H = \frac{\sigma_H}{e \cdot n_H} , \tag{8}$$

where σ_H is the proton conductivity, n_H is the proton concentration, and e is the elementary charge. As Figure 12b shows, with the introduction of the Co_3O_4 additive, the proton mobility increases. The activation energy (E_a) of the proton mobility is very close, 0.67 eV and 0.68 eV for $\text{La}_{0.95}\text{Ba}_{0.05}\text{ScO}_{3-\delta}$ and $\text{La}_{0.95}\text{Ba}_{0.05}\text{ScO}_{3-\delta} + 0.5 \text{ wt\% Co}_3\text{O}_4$, respectively.

3.6.3. Bulk and GB Conductivity

The conductivity of the bulk and grain boundaries (GB) of the $\text{La}_{0.95}\text{Ba}_{0.05}\text{ScO}_{3-\delta}$ and $\text{La}_{0.95}\text{Ba}_{0.05}\text{ScO}_{3-\delta} + 0.5 \text{ wt\% Co}_3\text{O}_4$ ceramics was measured in the temperature range 300–450 °C in a humidified oxidizing atmosphere using EIS. Figure 13a shows the typical impedance spectra of the samples studied, and Figure 13b shows the corresponding equivalent circuits. Figure 13c shows the temperature dependences of bulk and GB conductivity, and in Figure 13d, they are shown as $\sigma_{GB}/\sigma_{Bulk}$ ratios. The difference between the GB and bulk conductivities of $\text{La}_{0.95}\text{Ba}_{0.05}\text{ScO}_{3-\delta}$ increases with decreased in temperature, resulting in the significant impact of the GB contribution. The bulk conductivity of the $\text{La}_{0.95}\text{Ba}_{0.05}\text{ScO}_{3-\delta} + 0.5 \text{ wt\% Co}_3\text{O}_4$ sample is an order of magnitude lower than that of

$\text{La}_{0.95}\text{Ba}_{0.05}\text{ScO}_{3-\delta}$. In terms of the $\sigma_{\text{GB}}/\sigma_{\text{Bulk}}$ ratios, the contribution of GB conductivity is larger in the $\text{La}_{0.95}\text{Ba}_{0.05}\text{ScO}_{3-\delta} + 0.5 \text{ wt\% Co}_3\text{O}_4$ sample. As shown in Table 3, the effective activation energy (E_a) for the bulk conductivity of $\text{La}_{0.95}\text{Ba}_{0.05}\text{ScO}_{3-\delta} + 0.5 \text{ wt\% Co}_3\text{O}_4$ have higher values compared to $\text{La}_{0.95}\text{Ba}_{0.05}\text{ScO}_{3-\delta}$, which indicates the negative effect of the sintering additive on the transfer of charge carriers. At the same time, the E_a values for GB conductivity are comparable.

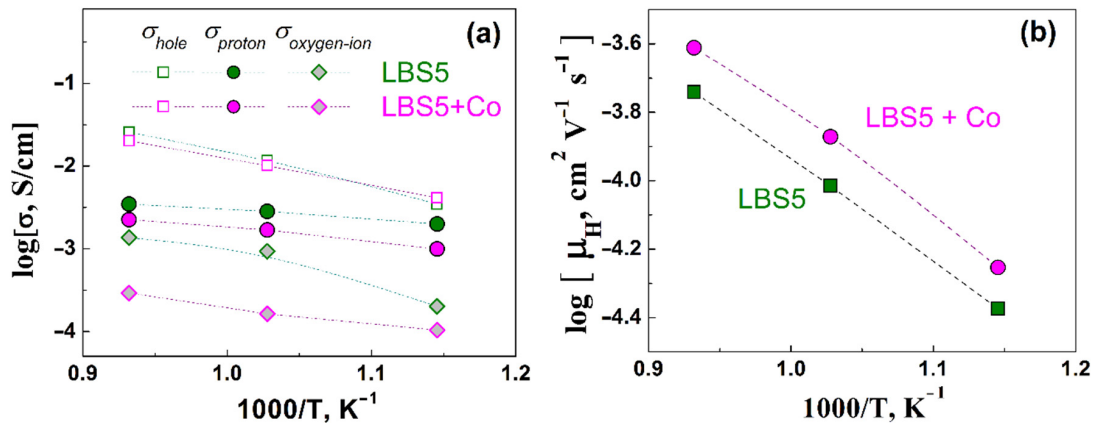


Figure 12. Temperature dependences of the proton, hole, and oxygen ion partial conductivities (a) and proton mobilities (b) of $\text{La}_{0.95}\text{Ba}_{0.05}\text{ScO}_{3-\delta}$ and $\text{La}_{0.95}\text{Ba}_{0.05}\text{ScO}_{3-\delta} + 0.5 \text{ wt\% Co}_3\text{O}_4$ samples.

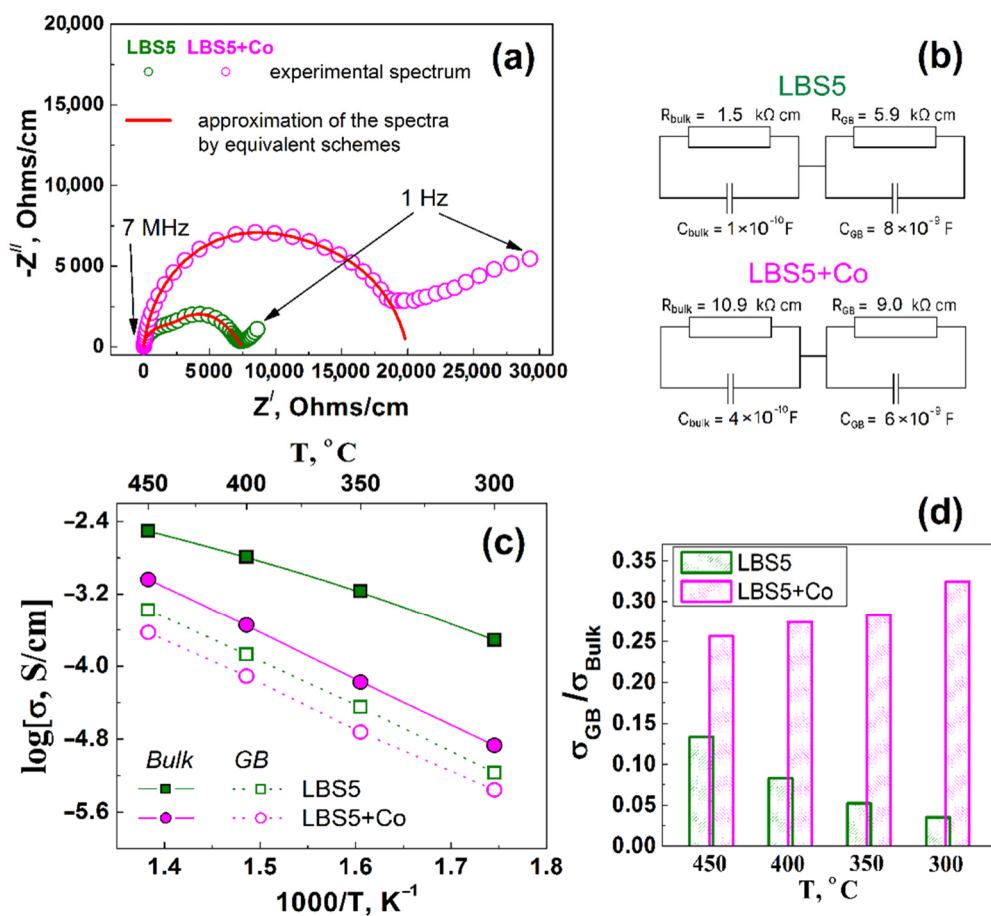


Figure 13. EIS results for $\text{La}_{0.95}\text{Ba}_{0.05}\text{ScO}_{3-\delta}$ and $\text{La}_{0.95}\text{Ba}_{0.05}\text{ScO}_{3-\delta} + 0.5 \text{ wt\% Co}_3\text{O}_4$ ceramics: (a) impedance spectra at 350 °C, (b) equivalent schemes, (c) temperature dependences of the bulk and GB conductivities, (d) $\sigma_{\text{GB}}/\sigma_{\text{Bulk}}$ ratios.

Table 3. Effective activation energies of the bulk and GB conductivity of $\text{La}_{0.95}\text{Ba}_{0.05}\text{ScO}_{3-\delta}$ and $\text{La}_{0.95}\text{Ba}_{0.05}\text{ScO}_{3-\delta} + 0.5 \text{ wt\% Co}_3\text{O}_4$ ceramics.

Conductivity	LBS	LBS + Co
Bulk	0.62 eV	0.89 eV
GB	0.98 eV	0.95 eV

4. Discussion

Despite the fact that the homogeneity region of $\text{La}_{1-x}\text{Ba}_x\text{ScO}_{3-\delta}$ solid solutions is located in a wide range up to $x \sim 0.4$ [15,31], an increase in the Ba content already leads to a significant decrease in the ceramic density in the $x \sim 0-0.1$ concentration range (Figure 2). We considered two strategies for obtaining dense $\text{La}_{0.95}\text{Ba}_{0.05}\text{ScO}_{3-\delta}$ ceramics: increasing the sintering temperature and introducing a sintering additive. It is understood that the sintering additive should promote both sintering due to a decrease in the material's melting temperature at the GBs and the incorporation of the dopant into the crystal lattice due to a decrease in carbonization of the Ba in the grains surface.

The production of dense $\text{La}_{0.95}\text{Ba}_{0.05}\text{ScO}_{3-\delta}$ ceramics without a sintering additive becomes possible only by high-temperature sintering in a vacuum at 1800°C . In this case, large grains with a size of $7.1 \pm 1.2 \mu\text{m}$ are formed (Figure 4c). The phase and chemical composition of the material correspond to the nominal ones thanks to the use of sacrificial coating powder, which prevents the evaporation of components, primarily Ba. In addition, no structural transitions were found in $\text{La}_{0.95}\text{Ba}_{0.05}\text{ScO}_{3-\delta}$ up to 900°C , according to HT-XRD analysis (Figure 9).

In the case of the Co_3O_4 sintering additive in $\text{La}_{0.95}\text{Ba}_{0.05}\text{ScO}_{3-\delta}$, the XRD and SEM results give us complex data. As SEM-EDX analysis in Figure 7b shows, the addition of 0.5 wt% Co_3O_4 in $\text{La}_{0.95}\text{Ba}_{0.05}\text{ScO}_{3-\delta}$ results in the release of a small amount of Sc_2O_3 , which is not detected by XRD [31]. The results of XRD analysis indicate partial decomposition of the material with the formation of $\text{Ba}_2\text{Sc}_2\text{O}_5$ and BaO_2 phases with a total mass fraction of about 1.5 wt%. Similarly, the formation of impurity phases in $\text{Ba}(\text{Ce,Zr,Y})\text{O}_{3-\delta}$ with Fe_2O_3 and NiO sintering additives was observed in a number of works [36,55–57]. EDX analysis of the cross sections does not detect these phases, which may be due to their small size and uniform distribution. A similar situation was obtained by Shakel et al. [56] for $\text{BaZr}_{0.8}\text{Y}_{0.2}\text{O}_{3-\delta}$ with NiO sintering additive, indicating that even transmission electron microscopy does not detect impurity phases in the form of individual grains. The XPS results in Figure 8 indicate that the Co content on the grain surface of the $\text{La}_{0.95}\text{Ba}_{0.05}\text{ScO}_{3-\delta} + 0.5 \text{ wt\% Co}_3\text{O}_4$ material is negligible, confirming that Co atoms diffuse into the bulk of the grains. In addition, a noticeable part of Ba is displaced to the surface of the grains, which reduces its concentration in the grain volume. Thus, this should lead to a decrease in the concentration of oxygen vacancies formed when La is replaced by Ba in accordance with Equation (1). However, the actual concentration of Ba in the volume of the $\text{La}_{0.95}\text{Ba}_{0.05}\text{ScO}_{3-\delta} + 0.5 \text{ wt\% Co}_3\text{O}_4$ sample grains corresponds to 0.048 according to EXD of the ceramics' cross-sections (Table 2), which indicates a small contribution of Ba segregation towards the GBs.

A small amount of 0.5 wt% Co_3O_4 additive cannot explain the significant decrease in the ionic conductivity of the material, as well as the water uptake, only due to the binding of Ba to the Co. In addition, an increase in the Ba dopant concentration at a constant of Co_3O_4 sintering additive concentration leads to an increase in the precipitation of the Sc_2O_3 phase (Figure S3). The general stoichiometry of $\text{La}_{0.95}\text{Ba}_{0.05}\text{ScO}_{3-\delta}$ is obviously violated when the sintering additive is introduced, which leads to partial decomposition of the material, in particular, the formation of Ba-enriched phases. Recently, Huang et al. [35] listed a number of effects from the introduction of a NiO sintering additive into BaZrO_3 -type materials. Violation of the cationic stoichiometry can cause the formation of cationic vacancies. Being a charged defect, cation vacancies can form associates with oxygen vacancies, which significantly reduces their mobility [56,58]. Additional trapping of oxygen vacancies is possible by Co atoms, which are embedded in Sc positions. Recent molecular

dynamics modeling confirms the possibility of the association of Co with oxygen vacancies in $\text{La}_{0.9}\text{Sr}_{0.1}\text{Sc}_{1-y}\text{Co}_y\text{O}_{3-\delta}$ [59]. Thus, some of the oxygen vacancies that form in accordance with Equation (1) and are directly related to the Ba dopant concentration may be associated with other defects and not participate in the oxygen ionic conductivity or water uptake reaction (Equation (2)).

The reduced oxygen vacancy content obviously reduces the saturation limit during hydration (x_{ef}). As Figure 9 shows, x_{ef} noticeably decreases from 0.048 for the sample without the sintering additive to 0.018 for the sample with the sintering additive. Apparently, it leads to a significant deterioration in proton transport (Figure 12a). It is fair to assume that Co atoms are partially included in the Sc site of the $\text{La}_{0.95}\text{Ba}_{0.05}\text{ScO}_{3-\delta}$ crystal lattice, displacing part of the Sc atoms and forming the $\text{La}_{0.95}\text{Ba}_{0.05}\text{Sc}_{1-y}\text{Co}_y\text{O}_{3-\delta}$ phase. Since Co can have an oxidation state of either +2 or +3, it can serve as a source of additional holes. The transfer of electron holes to oxygen atoms will lower the 'basicity' of oxygen sites [60]; in other words, it reduces the effective negative charge on oxygen atoms. This assumption is directly confirmed by the fact that the value of the standard enthalpy of hydration for $\text{La}_{0.95}\text{Ba}_{0.05}\text{ScO}_{3-\delta} + 0.5 \text{ wt}\% \text{Co}_3\text{O}_4$ ($\Delta H_{\text{hydr}} = -62 \text{ kJ mol}^{-1}$) becomes more positive compared to $\text{La}_{0.95}\text{Ba}_{0.05}\text{ScO}_{3-\delta}$ ($\Delta H_{\text{hydr}} = -85 \text{ kJ mol}^{-1}$), and thus, hydration becomes less favorable. This effect also leads to an increase in the mobility of protons in $\text{La}_{0.95}\text{Ba}_{0.05}\text{ScO}_{3-\delta} + 0.5 \text{ wt}\% \text{Co}_3\text{O}_4$ compared to $\text{La}_{0.95}\text{Ba}_{0.05}\text{ScO}_{3-\delta}$ (Figure 12b). On the other hand, Kim et al. [61] mention a decrease in the mobility of protons when Ni is introduced into $\text{BaZr}_{0.8}\text{Y}_{0.2}\text{O}_{3-\delta}$, which can be caused by the trapping of protons near Ni atoms.

The introduction of Co in $\text{La}_{0.95}\text{Ba}_{0.05}\text{ScO}_{3-\delta}$ leads to a slight decrease in the negative contribution of the GB resistance (Figure 13d). As well, the effective activation energy of GB conductivity for $\text{La}_{0.95}\text{Ba}_{0.05}\text{ScO}_{3-\delta}$ (0.98 eV) is higher than for $\text{La}_{0.95}\text{Ba}_{0.05}\text{ScO}_{3-\delta} + 0.5 \text{ wt}\% \text{Co}_3\text{O}_4$ (0.95 eV). The positive effect of the introduction of sintering additives was previously also mentioned by the authors [62–64] for $\text{Ba}(\text{Ce},\text{Zr})\text{O}_3$ -based materials with NiO, CuO, ZnO, Co_3O_4 sintering additives and is associated simply with an improvement in the contact between grains. Some authors [65,66] explained the decrease in the GB resistance by pointing to an increase in the concentration of charge carriers in the space charge layers and with lower potential transfer barrier. Most likely, this is facilitated by an increase in the transport numbers of holes (Figure 12a). The negative effect on the specific GB conductivity of $\text{Ba}(\text{Zr},\text{Y})\text{O}_3$ with the NiO additive [56,67] is associated with the blocking of ion transfers through the grain boundaries, whereas in our case, no such effect is observed.

5. Conclusions

The Ba dopant in $\text{La}_{1-x}\text{Ba}_x\text{ScO}_{3-\delta}$ causes deterioration of ceramic sintering already at low concentrations of $x = 0.025\text{--}0.1$, leading to a sharp decrease in the ceramic density up to 76% after sintering at 1650 °C for 5 h, as well as a decrease in the average grain size from 0.97 to 0.34 μm . Two strategies have been applied for obtaining dense ceramics: high processing temperatures and the introduction of a Co_3O_4 sintering additive. The use of 0.5 wt% Co_3O_4 sintering additive, despite its low concentration, caused a number of negative consequences. The set of methods used indicates a violation of the overall stoichiometry of the material and the formation of impurity phases: $\text{Ba}_2\text{Sc}_2\text{O}_5$, BaO_2 , and Sc_2O_3 . A significant deterioration in the ionic conductivity of the material may indicate an association of cationic and oxygen vacancies, which excludes the latter from oxygen transport and water uptake. The incorporation of Co into Sc positions causes a weakening of the binding energy of oxygen with a proton due to the transfer of electron holes from Co to oxygen. This causes an increase in the enthalpy of the hydration reaction and proton mobility. Thus, the use of sintering additives for LaScO_3 -based materials can lead to a number of negative consequences, since it significantly affects the actual concentration of the dopant and the cationic stoichiometry of the material. Highly dense ceramics (98%) can only be obtained by high-temperature sintering at 1800 °C, which also leads to a significant

increase in the average grain size to 7.08 μm . The accordance with the concentration of elements of the nominal composition is achieved by covering the materials with a protective powder of a similar composition, which, in particular, prevents Ba evaporation. The obtained electrolyte membranes demonstrate high water uptake and proton conductivity.

Supplementary Materials: The following supporting information can be downloaded at: <https://www.mdpi.com/article/10.3390/membranes12111084/s1>, Figure S1: Conductivity of ceramics as a function of $(p\text{O}_2)^{1/4}$ under wet ($p\text{H}_2\text{O} = 2.8$ kPa) and dry ($p\text{H}_2\text{O} = 0.1$ kPa) conditions; Figure S2: La3d and Sc2p core-level spectra La_{0.95}Ba_{0.05}ScO_{3- δ} + 0.5 wt% Co₃O₄ and La_{0.9}Sr_{0.1}ScO_{3- δ} + 0.5 wt% Co₃O₄ samples; Figure S3: SEM-images of the surface (a) and cross-sections (b) of La_{0.925}Ba_{0.075}ScO_{3- δ} + 0.5 wt% Co₃O₄ and La_{0.9}Ba_{0.1}ScO_{3- δ} + 0.5 wt% Co₃O₄ ceramics with EDX maps of cations distribution.

Author Contributions: Methodology, S.B. and A.K.; validation, A.L., S.B., S.P. and V.K.; investigation, A.L., S.B., A.S., S.P. and V.K.; data curation, A.K.; writing—Original draft preparation, A.L. and S.B.; writing—review and editing, S.P., V.K. and A.K.; visualization, A.L. and A.S.; supervision, A.K. All authors have read and agreed to the published version of the manuscript.

Funding: This research received no external funding.

Institutional Review Board Statement: Not applicable.

Data Availability Statement: Not applicable.

Acknowledgments: The optical dilatometry, XRD, SEM/EDX, and TGA studies were performed using the facilities of the Shared Research Center «Composition of compounds» at Institute of High-temperature Electrochemistry UB RAS. The HR-XRD studies were performed using the facilities of the Shared Research Center «Ural-M» at Institute of Metallurgy UB RAS. The XPS measurements were performed using the facilities of the Shared Research Center “National center of investigation of catalysts” at Borekov Institute of Catalysis SB RAS. The authors are grateful to A. Khodimchuk and A. Farlenkov for their great contribution to the experiment organization.

Conflicts of Interest: The authors declare no conflict of interest. The funders had no role in the design of the study; in the collection, analyses, or interpretation of data; in the writing of the manuscript; or in the decision to publish the results.

References

1. Iwahara, H.; Esaka, T.; Uchida, H.; Maeda, N. Proton conduction in sintered oxides and its application to steam electrolysis for hydrogen production. *Solid State Ion.* **1981**, *3*, 359–363. [[CrossRef](#)]
2. Bonanos, N.; Knight, K.; Ellis, B. Perovskite solid electrolytes: Structure, transport properties and fuel cell application. *Solid State Ion.* **1995**, *79*, 161–170. [[CrossRef](#)]
3. Iwahara, H.; Asakura, Y.; Katahira, K.; Tanaka, M. Prospect of hydrogen technology using proton-conducting ceramics. *Solid State Ion.* **2004**, *168*, 299–310. [[CrossRef](#)]
4. Okuyama, Y.; Nagamine, S.; Nakajima, A.; Sakai, G.; Matsunaga, N.; Takahashi, F.; Kimata, K.; Oshima, T.; Tsuneyoshi, K. Proton-conducting oxide with redox protonation and its application to a hydrogen sensor with a self-standard electrode. *RSC Adv.* **2016**, *6*, 34019–34026. [[CrossRef](#)]
5. Sakai, T.; Isa, K.; Matsuka, M.; Kozai, T.; Okuyama, Y.; Ishihara, T.; Matsumoto, H. Electrochemical hydrogen pumps using Ba doped LaYbO₃ type proton conducting electrolyte. *Int. J. Hydrogen Energy* **2013**, *38*, 6842–6847. [[CrossRef](#)]
6. Duan, C.; Huang, J.; Sullivan, N.; O’Hayre, R. Proton-conducting oxides for energy conversion and storage. *Appl. Phys. Rev.* **2020**, *7*, 011314. [[CrossRef](#)]
7. Medvedev, D.A. Current drawbacks of proton-conducting ceramic materials: How to overcome them for real electrochemical purposes. *Curr. Opin. Green Sustain. Chem.* **2021**, *32*, 100549. [[CrossRef](#)]
8. Kuzmin, A.V.; Lesnichyova, A.S.; Tropin, E.S.; Stroeve, A.Y.; Vorotnikov, V.A.; Solodyankina, D.M.; Belyakov, S.A.; Plekhanov, M.S.; Farlenkov, A.S.; Osinkin, D.A.; et al. LaScO₃-based electrolyte for protonic ceramic fuel cells: Influence of sintering additives on the transport properties and electrochemical performance. *J. Power Sources* **2020**, *446*, 228255. [[CrossRef](#)]
9. Nomura, K.; Tanase, S. Electrical behavior in (La_{0.9}Sr_{0.1})MO_{3- δ} (M = Al, Ga, Sc, In, and Lu) perovskite. *Solid State Ion.* **1997**, *98*, 229–236. [[CrossRef](#)]
10. Fujii, H.; Katayama, Y.; Shimura, T.; Iwahara, H. Protonic Conduction in perovskite-type Oxide Ceramics Based on LnScO₃ (Ln = La, Nd, Sm or Gd) at High Temperature. *J. Electroceram.* **1998**, *2*, 119–125. [[CrossRef](#)]
11. Lybye, D.; Poulsen, F.-W.; Mogensen, M. Conductivity of A- and B-site doped LaAlO₃, LaGaO₃, LaScO₃ and LaInO₃ perovskites. *Solid State Ion.* **2000**, *128*, 91–103. [[CrossRef](#)]

12. Nomura, K.; Takeuchi, T.; Tanase, S.; Kageyama, H.; Tanimoto, K.; Miyazaki, Y. Proton conduction in $(\text{La}_{0.9}\text{Sr}_{0.1})\text{M}^{\text{III}}\text{O}_{3-\delta}$ ($\text{M}^{\text{III}} = \text{Sc, In, and Lu}$) perovskites. *Solid State Ion.* **2002**, *154*, 647–652. [[CrossRef](#)]
13. Kato, H.; Kudo, T.; Naito, H.; Yugami, H. Electrical conductivity of Al-doped $\text{La}_{1-x}\text{Sr}_x\text{ScO}_3$ perovskite-type oxides as electrolyte materials for low-temperature SOFC. *Solid State Ion.* **2003**, *159*, 217–222. [[CrossRef](#)]
14. Nomura, K.; Takeuchi, T.; Kamo, S.; Kageyama, H.; Miyazaki, Y. Proton conduction in doped LaScO_3 perovskites. *Solid State Ion.* **2004**, *175*, 553–555. [[CrossRef](#)]
15. Lee, K.H.; Kim, H.L.; Kim, S.; Lee, H.L. Phase formation and electrical conductivity of Ba-doped LaScO_3 . *Jpn. J. Appl. Phys.* **2005**, *44*, 5025–5029. [[CrossRef](#)]
16. Gorelov, V.P.; Stroeva, A.Y. Solid proton conducting electrolytes based on LaScO_3 . *Russ. J. Electrochem.* **2012**, *48*, 949–960. [[CrossRef](#)]
17. Okuyama, Y.; Kozai, T.; Sakai, T.; Matsuka, M.; Matsumoto, H. Proton transport properties of $\text{La}_{0.9}\text{M}_{0.1}\text{YbO}_{3-\delta}$ ($\text{M} = \text{Ba, Sr, Ca, Mg}$). *Electrochim. Acta* **2013**, *95*, 54–59. [[CrossRef](#)]
18. Okuyama, Y.; Kozai, T.; Ikeda, S.; Matsuka, M.; Sakaid, T.; Matsumoto, H. Incorporation and conduction of proton in Sr-doped LaMO_3 ($\text{M} = \text{Al, Sc, In, Yb, Y}$). *Electrochim. Acta* **2014**, *125*, 443–449. [[CrossRef](#)]
19. Farlenkov, A.S.; Smolnikov, A.G.; Ananyev, M.V.; Khodimchuk, A.V.; Buzlukov, A.L.; Kuzmin, A.V.; Porotnikova, N.M. Local disorder and water uptake in $\text{La}_{1-x}\text{Sr}_x\text{ScO}_{3-\delta}$. *Solid State Ion.* **2017**, *306*, 82–88. [[CrossRef](#)]
20. Kuzmin, A.V.; Stroeva, A.Y.; Gorelov, V.P.; Novikova, Y.V.; Lesnichyova, A.S.; Farlenkov, A.S.; Khodimchuk, A.V. Synthesis and characterization of dense proton-conducting $\text{La}_{1-x}\text{Sr}_x\text{ScO}_{3-\alpha}$ ceramics. *Int. J. Hydrogen Energy* **2019**, *44*, 1130–1138. [[CrossRef](#)]
21. Lesnichyova, A.; Stroeva, A.; Belyakov, S.; Farlenkov, A.; Shevyrev, N.; Plekhanov, M.; Khromushin, I.; Aksenova, T.; Ananyev, M.; Kuzmin, A. Water Uptake and Transport Properties of $\text{La}_{1-x}\text{Ca}_x\text{ScO}_{3-\alpha}$ Proton-Conducting Oxides. *Materials* **2019**, *12*, 2219. [[CrossRef](#)] [[PubMed](#)]
22. Farlenkov, A.S.; Khodimchuk, A.V.; Shevyrev, N.A.; Stroeva, A.Y.; Fetisov, A.V.; Ananyev, M.V. Oxygen isotope exchange in proton-conducting oxides based on lanthanum scandates. *Int. J. Hydrogen Energy* **2019**, *44*, 26577–26588. [[CrossRef](#)]
23. Farlenkov, A.S.; Zhuravlev, N.A.; Denisova, T.A.; Ananyev, M.V. Interaction of O_2 , H_2O and H_2 with proton-conducting oxides based on lanthanum scandates. *Int. J. Hydrogen Energy* **2019**, *44*, 26419–26427. [[CrossRef](#)]
24. Lesnichyova, A.S.; Belyakov, S.A.; Stroeva, A.Y.; Kuzmin, A.V. Proton conductivity and mobility in Sr-doped LaScO_3 perovskites. *Ceram. Int.* **2021**, *47*, 6105–6113. [[CrossRef](#)]
25. Hyodo, J.; Kato, S.; Ida, S.; Ishihara, T.; Okuyama, Y.; Sakai, T. Determination of Oxide Ion Conductivity in Ba-Doped LaYbO_3 Proton-Conducting Perovskites via an Oxygen Isotope Exchange Method. *J. Phys. Chem. C* **2021**, *125*, 1703–1713. [[CrossRef](#)]
26. Kasyanova, A.V.; Lyagaeva, J.G.; Farlenkov, A.S.; Vylkov, A.I.; Plaksin, S.V.; Medvedev, D.A.; Demin, A.K. Densification, morphological and transport properties of functional $\text{La}_{1-x}\text{Ba}_x\text{YbO}_{3-\delta}$ ceramic materials. *J. Eur. Ceram. Soc.* **2020**, *40*, 78–84. [[CrossRef](#)]
27. Obukuro, Y.; Okuyama, Y.; Sakai, G.; Matsushima, S. Experimental and theoretical approaches for the investigation of proton conductive characteristics of $\text{La}_{1-x}\text{Ba}_x\text{YbO}_{3-\delta}$. *J. Alloys Compd.* **2019**, *770*, 294–300. [[CrossRef](#)]
28. Iwahara, H.; Uchida, H.; Ono, K.; Ogaki, K. Proton Conduction in Sintered Oxides Based on BaCeO_3 . *J. Electrochem. Soc.* **1988**, *135*, 529–533. [[CrossRef](#)]
29. Iwahara, H.; Yajima, T.; Hibino, T.; Ozaki, K.; Suzuki, H. Protonic conduction in calcium, strontium and barium zirconates. *Solid State Ion.* **1993**, *61*, 65–69. [[CrossRef](#)]
30. Kochetova, N.; Animitsa, I.; Medvedev, D.; Demin, A.; Tsiakaras, P. Recent activity in the development of proton conducting oxides for high-temperature applications. *RSC Adv.* **2016**, *6*, 73222–73268. [[CrossRef](#)]
31. Kendrick, E.; Knight, K.S.; Islam, M.S.; Slater, P.R. Structural studies of the proton conducting perovskite $\text{La}_{0.6}\text{Ba}_{0.4}\text{ScO}_{2.8}$. *Solid State Ion.* **2007**, *178*, 943–949. [[CrossRef](#)]
32. Loureiro, F.J.A.; Nasani, N.; Srinivas Reddy, G.; Munirathnam, N.R.; Fagg, D.P. A review on sintering technology of proton conducting BaCeO_3 - BaZrO_3 perovskite oxide materials for Protonic Ceramic Fuel Cells. *J. Power Sources* **2019**, *438*, 226991. [[CrossRef](#)]
33. Han, D.; Otani, Y.; Goto, K.; Uemura, S.; Majima, M.; Uda, T. Electrochemical and structural influence on $\text{BaZr}_{0.8-x}\text{Ce}_x\text{Y}_{0.2}\text{O}_{3-\delta}$ from manganese, cobalt, and iron oxide additives. *J. Am. Ceram. Soc.* **2020**, *103*, 346–355. [[CrossRef](#)]
34. Han, D.; Goto, K.; Majima, M.; Uda, T. Proton Conductive $\text{BaZr}_{0.8-x}\text{Ce}_x\text{Y}_{0.2}\text{O}_{3-\delta}$: Influence of NiO Sintering Additive on Crystal Structure, Hydration Behavior, and Conduction Properties. *ChemSusChem* **2021**, *14*, 614–623. [[CrossRef](#)]
35. Huang, Y.; Merkle, R.; Maier, J. Effect of NiO addition on proton uptake of $\text{BaZr}_{1-x}\text{Y}_x\text{O}_{3-x/2}$ and $\text{BaZr}_{1-x}\text{Sc}_x\text{O}_{3-x/2}$ electrolytes. *Solid State Ion.* **2020**, *347*, 115256. [[CrossRef](#)]
36. Huang, Y.; Merkle, R.; Maier, J. Effects of NiO addition on sintering and proton uptake of $\text{Ba}(\text{Zr,Ce,Y})\text{O}_{3-\delta}$. *J. Mater. Chem. A* **2021**, *9*, 14775–14785. [[CrossRef](#)]
37. Kuroha, T.; Niina, Y.; Shudo, M.; Sakai, G.; Matsunaga, N.; Goto, T.; Yamauchi, K.; Mikami, Y.; Okuyama, Y. Optimum dopant of barium zirconate electrolyte for manufacturing of protonic ceramic fuel cells. *J. Power Sources* **2021**, *506*, 230134. [[CrossRef](#)]
38. DIFFRACPlus: Eva Bruker AXS GmbH, Ostliche; Rheinbruckenstraße 50, D-76187: Karlsruhe, Germany. 2008. Available online: <https://www.bruker.com/en/products-and-solutions/diffractometers-and-scattering-systems/x-ray-diffractometers/diffrac-suite-software/diffrac-eva.html> (accessed on 15 September 2022).

39. Gates-Rector, S.; Blanton, T. The Powder Diffraction File: A Quality Materials Characterization Database. *Powder Diffr.* **2019**, *34*, 352–360. [[CrossRef](#)]
40. LMGP-Suite of Programs for the Interpretation of X-ray Experiments, by Jean Laugier and Bernard Bochu, ENSP/Laboratoire des Matériaux et du Génie Physique, BP 46. 38042 Saint Martin d'Hères, France. Available online: <http://www.inpg.fr/LMGP>; <http://www.ccp14.ac.uk/tutorial/lmgp/> (accessed on 24 June 2022).
41. Coelho, A.A. TOPAS and TOPAS-Academic: An optimization program integrating computer algebra and crystallographic objects written in C++. *J. Appl. Crystallogr.* **2018**, *51*, 210–218. [[CrossRef](#)]
42. Scofield, J.H. Hartree-Slater subshell photoionization cross-sections at 1254 and 1487 eV. *J. Electron Spectrosc. Relat. Phenom.* **1976**, *8*, 129–137. [[CrossRef](#)]
43. Fairley, N.; Fernandez, V.; Richard-Plouet, M.; Guillot-Deudon, C.; Walton, J.; Smith, E.; Flahaut, D.; Greiner, M.; Biesinger, M.; Tougaard, S.; et al. Systematic and collaborative approach to problem solving using X-ray photoelectron spectroscopy. *Appl. Surf. Sci. Adv.* **2021**, *5*, 100112. [[CrossRef](#)]
44. Frade, J.R. Theoretical behavior of concentration cells based on ABO₃ perovskite materials with protonic and oxygen-ion conduction. *Solid State Ion.* **1995**, *78*, 87–97. [[CrossRef](#)]
45. Baek, H.D. Modeling of electrical conductivity in high-temperature proton-conducting oxides. *Solid State Ion.* **1998**, *110*, 255–262. [[CrossRef](#)]
46. Guo, X.; Maier, J. Grain Boundary Blocking Effect in Zirconia: A Schottky Barrier Analysis. *J. Electrochem. Soc.* **2001**, *148*, E121–E126. [[CrossRef](#)]
47. Shannon, R.D. Revised effective ionic radii and systematic studies of interatomic distances in halides and chalcogenides. *Acta Crystallogr.* **1976**, *A32*, 751–767. [[CrossRef](#)]
48. Marrocchelli, D.; Perry, N.H.; Bishop, S.R. Understanding chemical expansion in perovskite-structured oxides. *Phys. Chem. Chem. Phys.* **2015**, *17*, 10028–10039. [[CrossRef](#)]
49. Omata, T.; Fuke, T.; Otsuka-Yao-Matsuo, S. Hydration behavior of Ba₂Sc₂O₅ with an oxygen-deficient perovskite structure. *Solid State Ion.* **2006**, *177*, 2447–2451. [[CrossRef](#)]
50. Chakrabarti, S.; Ginnaram, S.; Jana, S.; Wu, Z.Y.; Singh, K.; Roy, A.; Kumar, P.; Maikap, S.; Qiu, J.T.; Cheng, H.M.; et al. Negative voltage modulated multi-level resistive switching by using a Cr/BaTiO_x/TiN structure and quantum conductance through evidence of H₂O₂ sensing mechanism. *Sci. Rep.* **2017**, *7*, 4735. [[CrossRef](#)]
51. Alema, F.; Pokhodnya, K. Dielectric properties of BaMg_{1/3}Nb_{2/3}O₃ doped Ba_{0.45}Sr_{0.55}TiO₃ thin films for tunable microwave applications. *J. Adv. Dielectr.* **2016**, *05*, 1550030. [[CrossRef](#)]
52. Khassin, A.A.; Yurieva, T.M.; Kaichev, V.V.; Bukhtiyarov, V.I.; Budneva, A.A.; Paukshtis, E.A.; Parmon, V.N. Metal–support interactions in cobalt-aluminum co-precipitated catalysts: XPS and CO adsorption studies. *J. Mol. Catal. A Chem.* **2001**, *175*, 189–204. [[CrossRef](#)]
53. Biesinger, M.C.; Payne, B.P.; Grosvenor, A.P.; Lau, L.W.M.; Gerson, A.R.; Smart, R.S.C. Resolving surface chemical states in XPS analysis of first row transition metals, oxides and hydroxides: Cr, Mn, Fe, Co and Ni. *Appl. Surf. Sci.* **2011**, *257*, 2717–2730. [[CrossRef](#)]
54. Venezia, A.M.; Murania, R.; Pantaleo, G.; Deganello, G. Nature of cobalt active species in hydrodesulfurization catalysts: Combined support and preparation method effects. *J. Mol. Catal. A Chem.* **2007**, *271*, 238–245. [[CrossRef](#)]
55. Liu, Z.; Chen, M.; Zhou, M.; Cao, D.; Liu, P.; Wang, W.; Liu, M.; Huang, J.; Shao, J.; Liu, J. Multiple Effects of Iron and Nickel Additives on the Properties of Proton Conducting Yttrium-Doped Barium Cerate-Zirconate Electrolytes for High-Performance Solid Oxide Fuel Cells. *ACS Appl. Mater. Interfaces* **2020**, *12*, 50433–50445. [[CrossRef](#)] [[PubMed](#)]
56. Shakel, Z.; Loureiro, F.J.A.; Antunes, I.; Mikhalev, S.M.; Fagg, D.P. Tailoring the properties of dense yttrium-doped barium zirconate ceramics with nickel oxide additives by manipulation of the sintering profile. *Int. J. Energy Res.* **2022**, 1–12. [[CrossRef](#)]
57. Jennings, D.; Ricote, S.; Caicedo, J.M.; Santiso, J.; Reimanis, I. The effect of Ni and Fe on the decomposition of yttrium doped barium zirconate thin films. *Scr. Mater.* **2021**, *201*, 113948. [[CrossRef](#)]
58. Graça, V.C.D.; Loureiro, F.J.A.; Holz, L.I.V.; Mikhalev, S.M.; Fagg, D.P. Toward improved chemical stability of yttrium-doped barium cerate by the introduction of nickel oxide. *J. Am. Ceram. Soc.* **2022**, *105*, 6271–6283. [[CrossRef](#)]
59. Plekhanov, M.S.; Thomä, S.L.J.; Zobel, M.; Cuello, G.J.; Fischer, H.E.; Raskovalov, A.A.; Kuzmin, A.V. Correlating Proton Diffusion in Perovskite Triple-Conducting Oxides with Local and Defect Structure. *Chem. Mater.* **2022**, *34*, 4785–4794. [[CrossRef](#)]
60. Raimondi, G.; Giannici, F.; Longo, A.; Merkle, R.; Chiara, A.; Hoedl, M.F.; Martorana, A.; Maier, J. X-ray Spectroscopy of (Ba,Sr,La)(Fe,Zn,Y)O_{3-δ} Identifies Structural and Electronic Features Favoring Proton Uptake. *Chem. Mater.* **2020**, *32*, 8502–8511. [[CrossRef](#)]
61. Kim, E.; Yamazaki, Y.; Haile, S.M.; Yoo, H.-I. Effect of NiO sintering-aid on hydration kinetics and defect-chemical parameters of BaZr_{0.8}Y_{0.2}O_{3-Δ}. *Solid State Ion.* **2015**, *275*, 23–28. [[CrossRef](#)]
62. Shimura, T.; Tanaka, H.I.; Matsumoto, H.; Yogo, T. Influence of the transition-metal doping on conductivity of a BaCeO₃-based protonic conductor. *Solid State Ion.* **2005**, *176*, 2945–2950. [[CrossRef](#)]
63. Medvedev, D.A.; Murashkina, A.A.; Demin, A.K. Formation of dense electrolytes based on BaCeO₃ and BaZrO₃ for application in solid oxide fuel cells: The role of solid-state reactive sintering. *Rev. J. Chem.* **2015**, *5*, 193–214. [[CrossRef](#)]

64. Vdovin, G.K.; Rudenko, A.O.; Antonov, B.D.; Malkov, V.B.; Demin, A.K.; Medvedev, D.A. Manipulating the grain boundary properties of BaCeO₃-based ceramic materials through sintering additives introduction. *Chim. Technol. Acta* **2019**, *6*, 38–45. [[CrossRef](#)]
65. Heras-Juaristi, G.; Perez-Coll, D.; Mather, G.C. Effect of sintering conditions on the electrical-transport properties of the SrZrO₃-based protonic ceramic electrolyser membrane. *J. Power Sources* **2016**, *331*, 435–444. [[CrossRef](#)]
66. Nasani, N.; Shakel, Z.; Loureiro, F.J.A.; Panigrahi, B.B.; Kale, B.B.; Fagg, D.P. Exploring the impact of sintering additives on the densification and conductivity of BaCe_{0.3}Zr_{0.55}Y_{0.15}O_{3-δ} electrolyte for protonic ceramic fuel cells. *J. Alloys Compd.* **2021**, *862*, 158640. [[CrossRef](#)]
67. Ricote, S.; Bonanos, N.; Manerbino, A.; Sullivan, N.P.; Coors, W.G. Effects of the fabrication process on the grainboundary resistance in BaZr_{0.9}Y_{0.1}O_{3-δ}. *J. Mater. Chem. A* **2014**, *2*, 16107–16115. [[CrossRef](#)]